Transition metals vs. chalcogens: the impact on NO_x adsorption on MoS_2, $MoSe_2$ and WS_2 transition-metal dichalcogenides

Piotr Radomski[a], Maciej J. Szary[b,*]

[a]*Institute of Materials Research and Quantum Engineering, Poznan University of Technology, ul. Piotrowo 3, 61-138 Poznan, Poland*
[b]*Institute of Physics, Poznan University of Technology, ul. Piotrowo 3, 61-138 Poznan, Poland*

Abstract

The widely developed industry of today generates significant amounts of harmful gases, which prompts the search for modern materials allowing for their efficient and reliable detection. Transition-metal dichalcogenides (TMD) constitute well-known example of such, with particularly high potential for excellent sensing of NO_2. It is known, that the adsorption of this hazardous molecule varies on the TMD composition, however the importance of transition metal and chalcogen types were never previously contrasted. Moreover, the other NO_x compounds, namely NO and N_2, interact much less with TMD sheets, the reason for which is not yet well understood. This work utilizes density functional theory (DFT) approach to untangle these problems by examining the adsorption processes of NO_2, NO, and N_2 on the monolayers of WS_2, MoS_2, and $MoSe_2$. The calculations allowed to establish two important conclusions: (i) the chalcogen is significantly more important than transition metal, allowing for much greater increase in adsorption of NO_2 on $MoSe_2$ than on WS_2, as compared to that on MoS_2, (ii) only molecules acting as an acceptor with respect to the TMD sheet can benefit from the enhancement coming from the composition of the latter. The gained insight can likely contribute to the informed design of devices allowing selective detection, the lack of which is a recognized problem among semiconductor sensors.

Keywords: NO_2, MoS_2, transition metal dichalcogenides, surface interactions, adsorption, gas sensing,

1. Introduction

In recent decades, air pollution has emerged as a significant global challenge with detrimental impacts on both human health and the environment. Among the various air pollutants, nitrogen oxides (NO_x), encompassing nitrogen monoxide (NO) and nitrogen dioxide (NO_2), play a critical role in the formation of hazardous compounds and particulate matter [1–6]. These pollutants are primarily emitted from the combustion of fossil fuels in vehicles, industrial processes, and power plants. Upon inhalation, NO_x can cause a range of health issues, including respiratory problems, cardiovascular diseases, and exacerbation of existing respiratory conditions [7–10]. Additionally, NO_x contributes to the formation of acid rain and smog, leading to environmental degradation, ecosystem disruption, and subsequent economic costs [11–14]. To effectively address the adverse effects of NO_x pollution, it is crucial to develop comprehensive monitoring strategies that provide accurate and real-time data for assessing air quality and guiding targeted mitigation efforts [15]. Therefore, there is a pressing need to invest in the development of efficient and reliable monitoring techniques to combat this persistent challenge.

In a pursuit to enhance the detection efficiency of NO_x, considerable efforts have been devoted to exploring novel sensing materials, with transition-metal dichalcogenides (TMDs) emerging as promising candidates. TMDs exhibit unique physicochemical properties [16–20], coupled with an excellent surface-to-volume ratio, rendering them highly sensitive to molecule adsorption. This sensitivity results in measurable changes in their electronic and optical signals. Notably, recent studies have showcased the potential of TMDs for the highly sensitive and selective detection of NO_x gases in ambient air [21–23]. Furthermore, applying gate bias [24, 25], and using light illumination [26–28] have been reported effective in enhancing the overall performance of TMD-based sensors. Consequently, the utilization of TMD-based sensors holds the promise of revolutionizing air quality monitoring by offering cost-effective, low-power, and portable devices capable of real-time NO_x detection at room temperature. Nonetheless, challenges remain in terms of improving the selectivity, recovery, and response time of these sensors [29–31]. Further investigation and optimization of TMD-based gas sensing mechanisms hold the key to advancing this technology and addressing the pressing need for more robust and efficient NO_x monitoring strategies. In particular, the impact of comprising elements on the sensitivity of TMDs remains still elusive.

TMDs have a chemical formula of MX_2, with M a transition-metal atom (Mo, W, etc.) and X a chalcogen atom (S, Se, or Te). TMDs reported sensitive to NO_x, including molybdenum disulfide (MoS_2), molybdenum diselenide ($MoSe_2$), and tungsten disulfide (WS_2), favor trigonal-particle geometry with transition-metal atoms sandwiched between two layers of chalcogen. This makes sheets semiconducting [32], with most readily available donors of electrons on their surface being p_z orbitals of the chalcogens [18, 19]. Consequently, chalcogens comprising the TMDs could directly affects molecule-sheet interactions. On the other hand, M–X bonds could also play an important role in charge distribution in the sheet, and thus have some impact on the adsorption. This in turn, could affect the interaction between acceptor-type molecules and TMD sheets, thus impacting their sensitivity to NO_x.

The sensitivity of the sensor relies significantly on the charge transfer (δQ) occurring between the analyte and the sensing layer. This process directly impacts observable properties like conductivity and photoluminescence, making it feasible to detect gases. Conversely, the recovery of the sensor depends on the adsorption energy (E_{ads}) of the target species, as it governs desorption rates. Both of these crucial parameters can be accurately determined through computational quantum mechanical modeling. In this context, Zeng et al. [33] and Tang et al. [34] have explored the significance of computational studies in this field and highlighted their valuable contribution to gaining a quanti-

*Corresponding author
Email address: maciej.szary@put.poznan.pl (Maciej J. Szary)

tative understanding of adsorption and charge transfers. Subsequent studies [17, 20, 35–37] have further underscored the efficacy of such computational approaches.

As a result, this study utilizes density functional theory (DFT) methods to investigate the adsorption of NO_x and N_2 on the monolayers of MoS_2, $MoSe_2$, and WS_2. The primary objective is to compare how transition metals and chalcogens influence molecule-sheet interactions among the most widely studied TMDs and to consider the potential selectivity of those effects.

2. Computational Details

The entirety of the DFT calculations presented in this study utilzed plane-wave/psuedopotential (PW/PP) formalism along with the projector augmented wave (PAW) method executed using version 7.0 of Quantum ESPRESSO suite [38–40]. The employed pseudopotentials (PP) were of scalar-relativistic kind and included nonlinear core corrections. The Perdew-Burke-Ernzerhof (PBE) functional [41, 42] was implemented for approximating the electron exchange-correlation energy. Van der Waals (vdW) contributions were incorporated to the total energy with Grimme's D3 method [43, 44]. The selection of the PBE+D3 treatment was based on preliminary tests, including the Heyd-Scuseria-Ernzerhof (HSE) exchange-correlation functional [45] and Tkatchenko-Scheffl van der Waals vdW treatment [46]. These tests demonstrated that the PBE+D3 approach satisfactorily describes the electronic properties of TMD monolayers and the interactions on their surfaces, aligning with findings from prior studies [47–50]. Conducted calculations were spin-polarized with magnetization set along z axis. The PW cutoff energy was set to 55 Ry for the wave function and to 500 Ry for the electron density. Monkhorst–Pack (MP) [51] k-point grids of $6 \times 6 \times 1$ and $24 \times 24 \times 1$ were chosen for the 4×4 supercell and 1×1 cell respectively, along with a Gaussian smearing of 0.005 Ry for the integration of the surface Brillouin zone. Löwdin population analysis was performed to estimate partial charges. For the optimization of the total energy, the positions of all atoms were relaxed until the convergence criteria of $<10^{-3}$ Ry/au for the force and $<10^{-5}$ Ry for the total energy were reached.

To model the adsorption process each molecule was placed few Å above the two-dimensional (2D) periodic TMD slab with a 4×4 supercell as shown in Figure 1. About 25 Å of vertical vacuum space was inserted among repeated slabs. This approach was proven successful by previous works on similar systems [37, 48, 52]. As the adsorption occurs only on the upper surface of the sheet, the setup is asymmetric. Latter is evident through a dipole moment perpendicular to the slab, introduced as the consequence of electron transfer between the sheet and adsorbates. These circumstances in addition with the periodic boundary conditions result in an artificial electric field between neighboring slabs. Dipole correction layer (DCL) [53] was implemented in the middle of the vacuum space in order to compensate for the described effect. The width of the vacuum region was adjusted to contain the DCL while simultaneously not overlapping the adsorption and reaction region on top of the sheets. Figures 1, 2 and part of figure 8 were generated using the XcrySDen visualization program [54].

3. Results and Discussion

3.1. Adsorption of NO_x on layers of MoS_2, $MoSe_2$, and WS_2

The adsorption of analyte molecules on top of TMD layers generally occurs via vdW forces. This is a consequence of low chemical activity of TMD sheets and results in lack of sole, preferable adsorption configuration. As energies separating different configurations are relatively low and dominant interaction forces have dispersive character, an analyte can undergo transitions between semi-stable states and diffuse over the surface. The above behavior is exhibited even in relatively low temperatures. In order to investigate a system which displays the aforementioned properties, a range of adsorption configurations have to be used in a place of single, global minimum one. Therefore, this study utilizes a range of NO_x adsorption geometries differing in the orientation and position of the molecule. These configurations are made equivalent across all investigated sheets. Presented approach enable us to mitigate compounding adsorption effects which is of paramount importance as it allows for a clear and unambiguous description of the effects facilitated by transition metals and chalcogens.

In the present paper we have examined following molecules: N_2, NO, and NO_2. Initial configurations of foregoing placed above the MoS_2 layer are displayed by Figure 1. The subfigures (a–d) present NO_2 molecule in following initial configurations: (a) Horizontally situated NO_2 with the N atom placed above the chalcogen atom (HN); (b)

Table 1: Adsorption of NO_x on monolayer MoS_2, $MoSe_2$, and WS_2.

Sheet	Geometry	Figure	$-E_{ads}$ meV	$-\delta Q$ e	Δz Å	d_{min} Å
			NO_2			
WS_2	HN	2a	178	0.042	2.98	3.21
	HO	S1a	162	0.037	2.94	3.29
	VN	S2a	85	0.006	3.92	3.92
	VO	S3a	134	0.015	3.10	3.31
	avg.		140	0.025	3.24	3.43
MoS_2	HN	2b	172	0.041	2.99	3.22
	HO	S1b	157	0.036	2.90	3.31
	VN	S2b	82	0.005	3.93	3.93
	VO	S3b	129	0.014	3.11	3.31
	avg.		135	0.024	3.23	3.44
$MoSe_2$	HN	2c	205	0.070	2.98	3.21
	HO	S1c	190	0.087	2.89	3.24
	VN	S2c	145	0.058	3.11	3.12
	VO	S3c	145	0.046	3.16	3.35
	avg.		171	0.065	3.04	3.23
			NO			
WS_2	HN	2d	144	0.033	2.99	3.00
	HO	S1d	136	-0.012	3.14	3.37
	VN	S2d	87	-0.005	3.49	3.50
	VO	S3d	91	-0.003	3.46	3.46
	avg.		114	0.003	3.27	3.33
MoS_2	HN	2e	142	0.031	2.95	2.97
	HO	S1e	135	-0.015	3.14	3.36
	VN	S2e	95	-0.003	3.52	3.52
	VO	S3e	90	-0.002	3.45	3.45
	avg.		115	0.003	3.26	3.33
$MoSe_2$	HN	2f	154	0.049	3.04	3.06
	HO	S1f	132	-0.007	3.24	3.47
	VN	S2f	97	0.008	3.60	3.60
	VO	S3f	89	-0.001	3.58	3.59
	avg.		118	0.012	3.37	3.43
			N_2			
WS_2	H	2g, S1g	87	0.004	3.70	3.70
	V	S2g, S3g	60	0.001	3.62	3.63
	avg.		73	0.003	3.66	3.67
MoS_2	H	2h, S1h	87	0.005	3.51	3.60
	V	S2h, S3h	59	0.001	3.60	3.61
	avg.		73	0.003	3.56	3.60
$MoSe_2$	H	2i, S1i	87	0.005	3.62	3.69
	V	S2i, S3i	60	0.001	3.71	3.71
	avg.		73	0.003	3.67	3.70

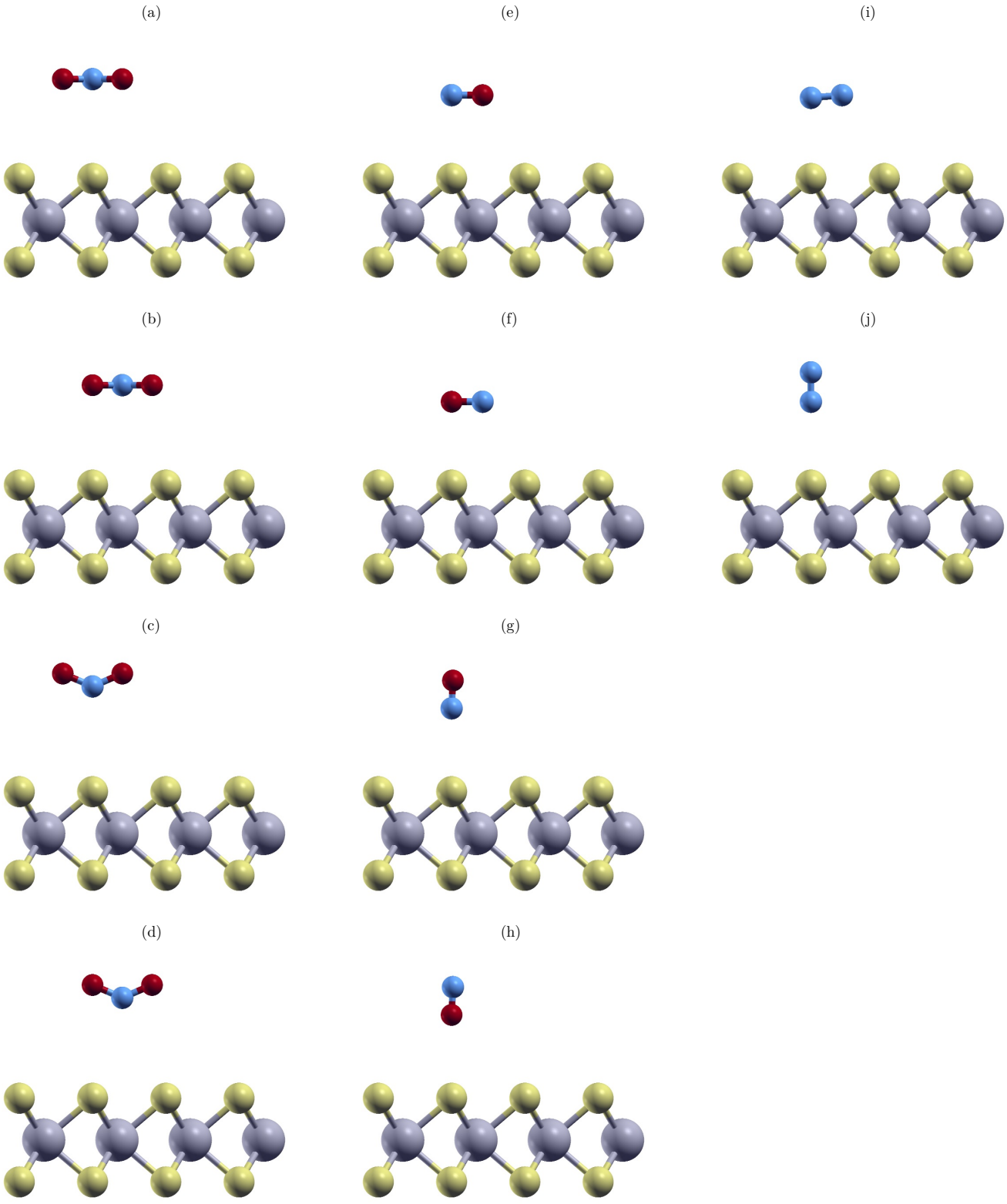

Figure 1: Schematic representation of initial adsorption geometries of NO_2 molecule (a–d): HN, HO, VN, and VO; NO molecule (e–h): HN, HO, VN, and VO; N_2 molecule (i–j): H, and V respectively. The illustrations depicts only sheet of MoS_2, as adsorption configurations of WS_2, and $MoSe_2$ systems are equivalent.

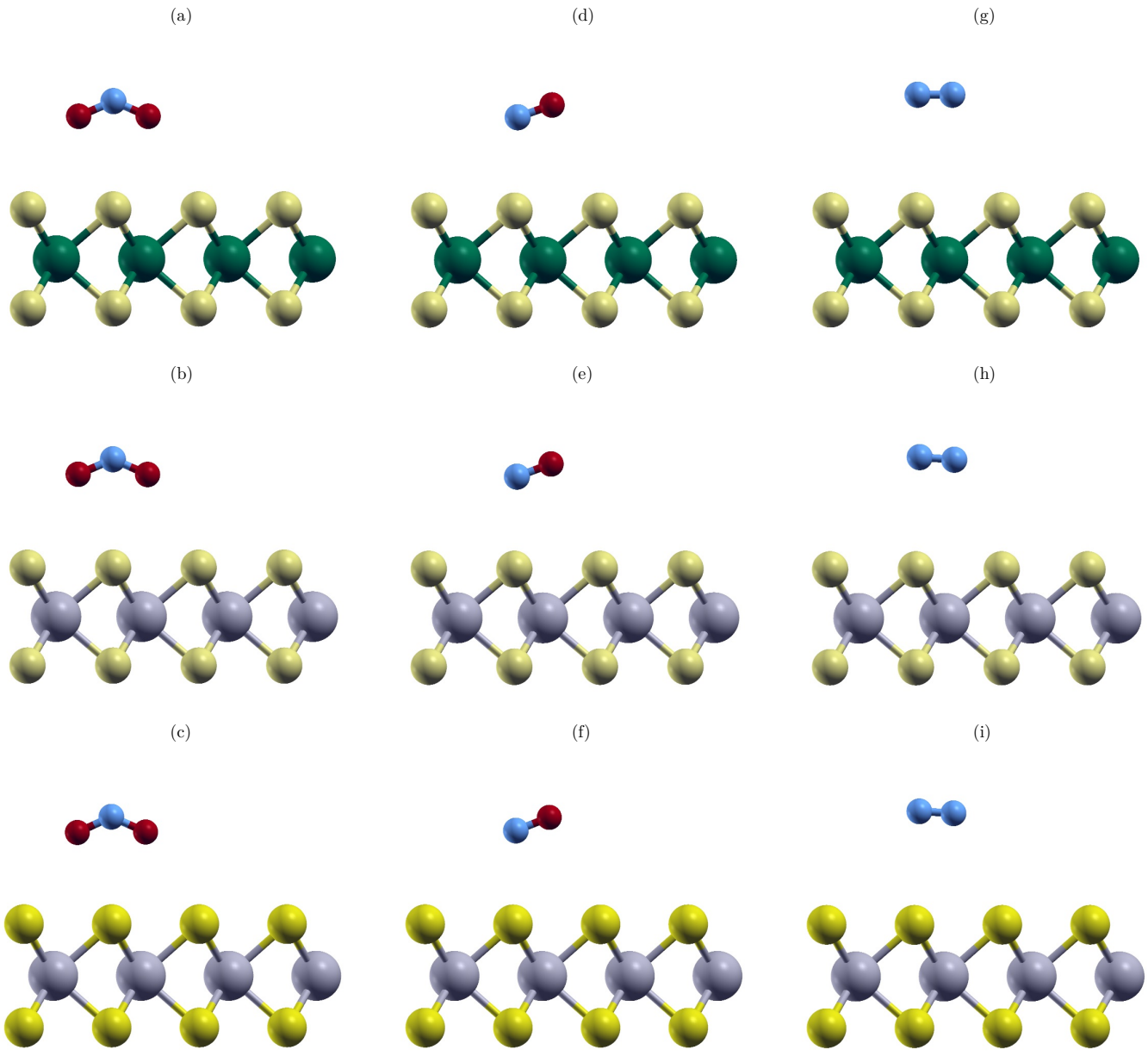

Figure 2: Optimized atomic structures of the most favorable adsorption configuration of (a) NO_2@WS_2, (b) NO_2@MoS_2, (c) NO_2@$MoSe_2$, (d) NO@WS_2, (e) NO@MoS_2, (f) NO@$MoSe_2$, (g) N_2@WS_2, (h) N_2@MoS_2, (i) N_2@$MoSe_2$. The remaining optimized structures are shown in the supplementary materials.

Horizontally situated NO_2 with the O atom placed above the chalcogen atom (HO); (c) Vertically situated NO_2 with the N atom placed above the chalcogen atom (VN); (d) Vertically situated NO_2 with the O atom placed above the chalcogen atom (VO). The subfigures (e–h) show NO molecule in geometries: (e) HN, (f) HO, (g) VN and (h) VO, all of which are analogous to the ones of NO_2. Finally, the N_2 configurations are of following: (i) Horizontally situated N_2 (H); (j) Vertically situated N_2 (V). The geometries of WS_2 and $MoSe_2$ systems are equivalent, therefore not shown. By employing presented approach we can obtain detailed description of adsorption, allowing us to recognize the differences depending on the TMD variety and dismiss the positioning associated effects.

One can quantitatively describe the process of adsorption by calculating corresponding energy defined as:

$$E_{\text{ads}} = E(\text{NO}_x\text{@TMD}) - E(\text{NO}_x) - E(\text{TMD}), \tag{1}$$

where $E(\text{NO}_x\text{@TMD})$, $E(\text{NO}_x)$, and $E(\text{TMD})$ are the total energy of the adsorbate-substrate system, free molecule, and the TMD monolayer respectively. Occurring charge transfer is evaluated by quantifying the net charge within the analyte:

$$\delta Q = Q(\text{adsorbed NO}_x) - Q(\text{free NO}_x). \tag{2}$$

where $Q(\text{adsorbed NO}_x)$ and $Q(\text{free NO}_x)$ are summed up per-orbital populations of the atoms forming accordingly adsorbed and free NO_x.

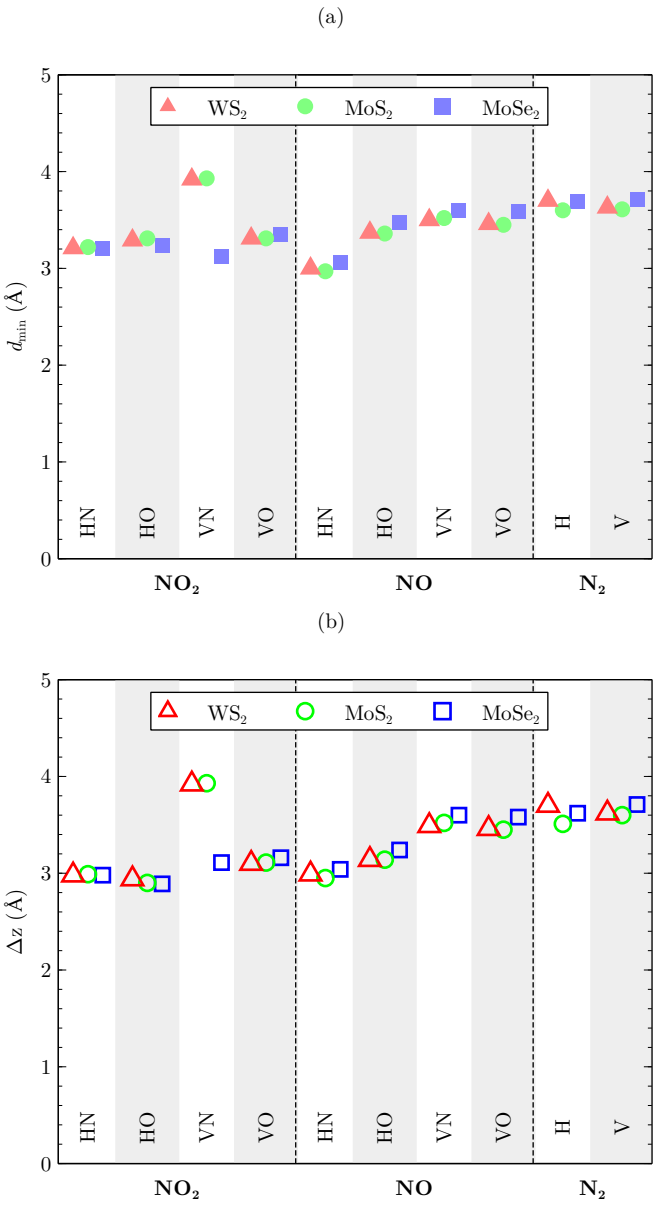

Figure 3: (a) Histograms illustrating minimum distance d_{min} between the closest atoms of NO_x and TMD as well as (b) difference Δz in z component between the lowest molecule atom and averaged z component of upper chalcogen layer for optimized structures. The HN, HO, VN, VO labels refer to initial geometry of a given NO_x@TMD system.

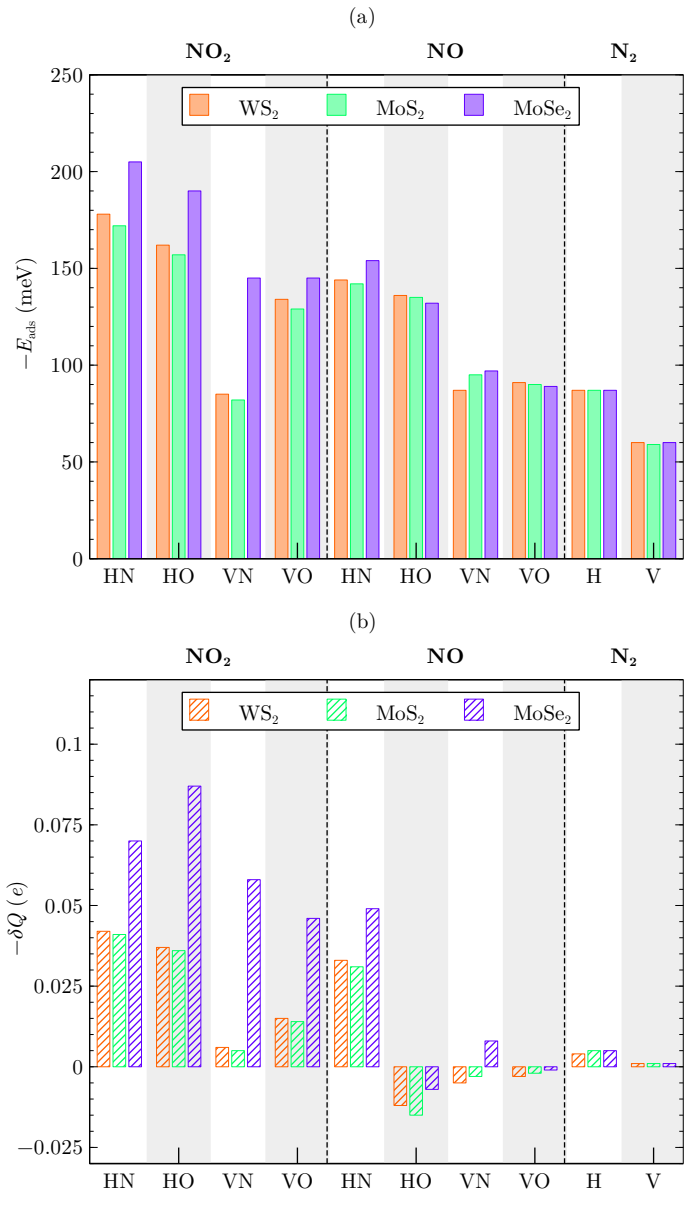

Figure 4: (a) Histograms portraying adsorption energy E_{ads} and (b) charge transfer δQ occurring from TMD layer to NO_x (b) as given by equations 1 and 2 respectively. The HN, HO, VN, VO labels refer to initial geometry of a NO_x@TMD system.

The values of adsorption energy and charge transfer are summarized in Table 1 alongside with the Δz and d_{min} parameters, which successively refer to a difference in z component between the lowest atom of a molecule and averaged z component of upper chalcogen layer, and minimum distance between analyte and the closest TMD atom. By inspecting the adsorption energy values it can be clearly seen that the most energetically favorable configuration of the molecules were all obtained from HN initial configurations for systems containing NO_2 or NO, and from H initial configurations for N_2 systems. These are therefore presented in Figure 2 with the remaining relaxed structures included in supplementary materials in Figures S1, S2, and S3.

The comparison of Fig 1 and Fig 2 shows that the final geometry of the adsorption systems depends to some extent on their initial conformation. However, upon closer inspection it is apparent that all of the relaxed conformations of a given molecule are quantitatively the same for each starting geometry, regardless of the type of TMD substrate. This can be demonstrated by mutually comparing subfigures (a–c) of Figure 2, as well as (d–f) or (g–i). Analogous can be observed by contrasting same-column images belonging to any of Figures S1, S2, and S3. Such results make up a promising base for a recognition of differences in the adsorption processes depending on the diversity of internal electronic structure of the TMDs and analytes and not on their geometrical arrangements. By the more detailed assessment of the relaxation data following behavior of NO_x can be highlighted: (i) the NO_2 always aligns itself vertically, with the O atoms facing downwards for the HO and HN and upwards for the VO and VN initial configurations, (ii) in the NO systems derived from horizontal initial configurations the

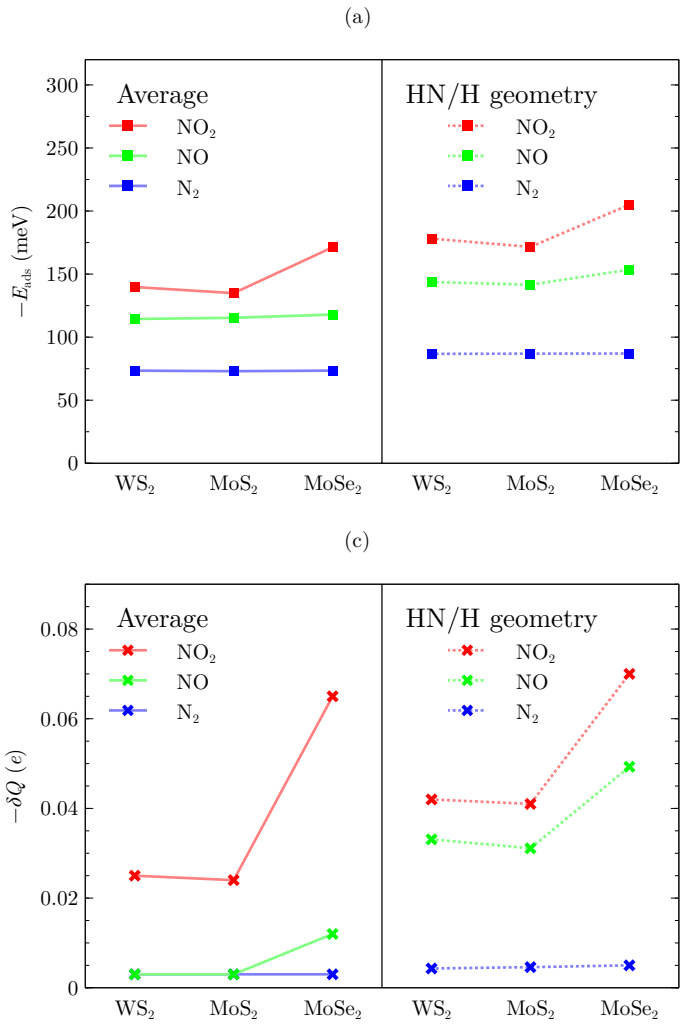

Figure 5: (a) Averaged adsorption energy E_{ads} and (b) charge transfer δQ values of a given NO_x@TMD system. Auxiliary E_{ads} and δQ graphs containing values coming from HN geometries are there to elucidate the case of NO molecule.

molecule slightly deflects as the O atom moves upwards, whereas for the VN NO@WS_2, VO NO@WS_2, and VO NO@MoS_2 the NO undergo minimal tilt and remains in approximately the same position in the rest of the vertical arrangements, (iii) in all the cases orientation of N_2 remains qualitatively unchanged with the exception of minor fluctuations. Exhibited behavior of the analytes is consistent with the previous reports [16, 17, 20, 48]. The achieved similarity of an adsorbate arrangement within its relaxed systems are of noticeable importance for benchmarking of dissimilarities between TMDs, as it allows for exclusion of geometry-related differences. Moreover, considered NO_x also behave mutually consistent, i.e. they all position themselves on comparable heights above a TMD sheet. The structural data regarding the molecules in relaxed configurations is exhibited in the form of scatter plots presented in Figure 3. Exact values are as recorded in Table 1. It can be seen in Figure 3a, that almost all of the minimal distances d_{min} are of similar values. The same is true for differences in vertical coordinate Δz between a sheet and a molecule, as it is displayed by Figure 3b. The only configurations which stand out are the two VN geometries of NO_2 i.e. NO_2@WS_2 VN and NO_2@MoS_2 VN. The deviation is seemingly pretty protruding, therefore it shall be closely investigated. The relaxations of the aforementioned systems have left NO_2 adsorbates roughly 0.9 Å higher above a TMD sheet than in the other cases, which can be concluded through Figure 3 and comparison of Figure S2a, b with Figure 2a–c, S1a–c, S2c and S3a–c. However, both of the inspected NO_2 remain its characteristic vertical orientation. Moreover, the O atoms belonging to them are directed upwards, just as for NO_2@$MoSe_2$ (cf. Figure S2a, b to c). These facts indicate that the distance surpluses result purely from a weaker molecule-sheet interaction and not from secondary effects, which is confirmed by the appropriately higher adsorption energy of NO_2@WS_2 VN and NO_2@MoS_2 VN (see Table 1). It is therefore suitable to include NO_2@WS_2 VN and NO_2@MoS_2 VN systems in further examinations. As the rest of the d_{min} and Δz data is of comparable quantity, we can safely proceed on to the analysis of adsorption energy and charge transfer.

Histograms presented in Figure 4 serve as a quantitative guide for the levels of adsorption energies (see Figure 4a) and charge transfers (see Figure 4b). Upon brief inspection it is prominent that the spread of values is huge as compared to the structural parameters plotted in Figure 3. The lowest E_{ads} values signifying the greatest adherence are of NO_2, followed successively by the ones of NO and finally of N_2. The δQ graph bears more complicated structure with the appearing negative transfers for NO molecule in the HO, VN and VO geometry. If a magnitude of electronic transfer is considered, the NO_x can be ordered in the same manner as for the adsorption energy, with the highest absolute values belonging to the NO_2 systems, followed by the NO and N_2 systems respectively. The strengths of adsorption interaction and charge transfer are both lower for the NO_2@WS_2 VN and NO_2@MoS_2 VN, nonetheless it is completely natural as their optimal positions lie higher above a TMD layer as compared to the other NO_2 systems. In addition, as it was previously highlighted, the orientations of all relaxed NO_2 sharing the same initial geometry remain mutually consistent. Juxtaposing Figure 4a to Figure 3 shows that the total form of the E_{ads} histogram is not a solely consequence of differing d_{min} and Δz. Rather it seems to be connected with the magnitudes of δQ (cf. Figure 4a to Figure 4b). Nitrogen dioxide, which universally displays strong acceptor-like response, takes part in the highest transfers of charge and in all cases adsorbs the most to a TMD sheet. The weakest adsorption interaction is displayed by N_2, known for its reluctance to accept or donate charge, clearly visible also in this study. The acceptor-donor character of NO varies according to its orientation. For the single VN and all of the HN geometries the molecule accepts charge, acting like a donor in the rest of the cases. In result nitrogen monoxide finds itself in between NO_2 and N_2 with medial levels of E_{ads} and δQ. The above shows that for all of the NO_x the electronic transfer data excellently respond to that of adsorption energy.

Currently it may seem, that the intensities of the adsorption processes are governed purely by the capability of the molecule to participate in the charge transfer. Nevertheless, another important factor should be noted. Upon closer examination of the NO_2 it cannot be omitted that in all cases by far the strongest adsorption is exhibited by the systems including a layer of $MoSe_2$. The second greatest interaction between NO_2 and a TMD appears for WS_2, with the sheets of MoS_2 interacting a little less. Apparently, there exists some relationship of adsorption energy and the types of transition metal and chalcogen forming a TMD layer. The same dependence can be additionally observed for the HN geometry of NO. The rest of the values do not appear to be correlated with the TMD composition. In order to elucidate this interesting behavior the averaged E_{ads} and δQ were plotted as a functions of the substrate type and placed on the left side of Figure 5a and b respectively. The most scattered set of points describing adsorption energy and charge transfer of NO_2 blatantly stands in opposition to the practically straight line connecting points of N_2. The NO

related function stays somewhere in between, with the highest offset of averaged E_{ads} and δQ for $MoSe_2$. As it can be seen, the average adsorption graphs stay distinctly separated. However, the latter is not true for the averaged electronic transfers, which is due to not consistent behavior of NO. For this reason, the data related to the HN geometries of the molecules is additionally shown on the right side of the graphs, because for these NO always acts acceptor-like. In this way, the enhanced adsorption relation to the magnitude of charge withdrawn by acceptor molecules can be fully appreciated, as all of the δQ points are visibly separated and correlate to the values of E_{ads}.

The above observations highlight two important behaviors of the considered systems: (i) the selectivity of the enhanced adsorption interaction, depending on the characteristics of an analyte, and (ii) the existing relationship of enhancement magnitude with the composition of TMD. The reasons behind observed differences are by no means obvious. Each of the TMD adsorbents exhibits its hexagonal phase. Moreover, Mo and W atom both have identical number of valence electrons, which is also true for S and Se. Consequently, the WS_2, MoS_2 and $MoSe_2$ layers share the same symmetry simultaneously containing equal number of bonds, all of alike character. It is not unsubstantiated to expect a similar sheet-molecule interaction. How is it therefore possible for the adsorption to differ so much? The detailed answer to this question is presented in the two subsequent parts of this work: firstly, we inspect an origin of the selectivity, after which we proceed on to the analysis of the impact on adsorption induced by the TMD composition. The later also emphasize differences regarding to the type of transition metal as opposed to the chalcogen variety.

3.2. *Connection between the selectivity of the enhanced adsorption and the NO_x acceptability*

In order to explore the selectivity of adsorption it is fruitful to carefully examine the distinction in the behavior of the adsorbates. One way to achieve a quantitative comparison is to consider the differences in E_{ads}, related to the change of substrate. For a given NO_x molecule:

$$\Delta E_{ads}(\mathrm{TMD}^a, \mathrm{TMD}^b) = E_{ads}(\mathrm{NO_x@TMD}^a) - E_{ads}(\mathrm{NO_x@TMD}^b) \quad (3)$$

Analogous can be done for the charge transfers:

$$\Delta\delta Q(\mathrm{TMD}^a, \mathrm{TMD}^b) = \delta Q(\mathrm{NO_x@TMD}^a) - \delta Q(\mathrm{NO_x@TMD}^b) \quad (4)$$

Naturally, equations 3 and 4 should be limited to pairs of TMD layers differing by a single atom type, otherwise it would be difficult to acknowledge which substitution, the one of transition metal or of chalcogen, is responsible for the greatest changes. The differences were calculated for the averaged values as displayed in Figure 5. Obtained $\Delta\,\mathrm{avg.}\,E_{ads}(MoS_2, WS_2)$ and $\Delta\,\mathrm{avg.}\,E_{ads}(MoS_2, MoSe_2)$ are presented as histograms visible in Figure 6a, whereas the $\Delta\,\mathrm{avg.}\,\delta Q(MoS_2, WS_2)$ and $\Delta\,\mathrm{avg.}\,\delta Q(MoS_2, MoSe_2)$ are placed in Figure 6b. It is quite obvious, that the greatest enhancement of adsorption interaction is experienced by NO_2, with the decrease in E_{ads} of roughly 4.8 and 36.4 meV for Mo → W and S → Se swaps respectively. Much lesser improvement is observed for the NO, as it loses only about 0.9 meV for Mo → W and 2.6 meV for S → Se substitution. Finally, N_2 show almost no participation in the effect, as its regarding changes are almost equal with the values below 0.5 meV. Clearly, NO_2 benefits the most from the replacements in substrate composition. To understand why, it is necessary to first consider the the mechanism behind the physisorption on surfaces of TMD layers.

The examined sheets of TMD disclose a hexagonal symmetry, with every one of the metal atoms enclosed by six nearest-neighbor chalcogen atoms in a trigonal prismatic geometry, facilitated by sd^5 orbital hybridization. The adsorption of acceptor-type molecule on the layers

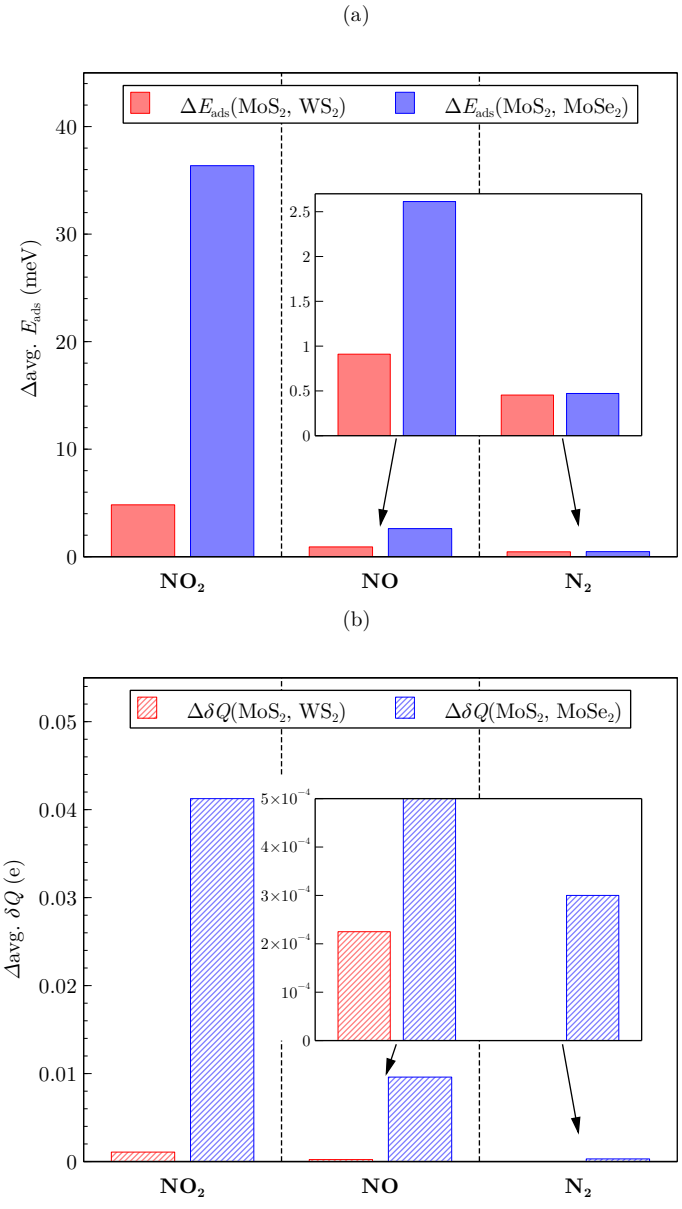

Figure 6: (a) Histograms presenting difference in average adsorption energy Δavg. E_{ads} and (b) charge transfer Δavg. δQ between same-molecule different-sheet adsorption systems as given by equations 3 and 4 respectively.

of such kind is mostly governed by the availability of the outward projected p_z orbitals of the chalcogens. The greater is the external electron charge density, the more electrons are available to undergo a charge transfer between the sheet and adsorbing analyte, resulting in a stronger binding. However, the level to which the charge is accessible on the surface is directly connected to the bonding of metal and chalcogen. The formation of M–X bond in TMD layer requires an electron transfer between M and X. This leads to charge redistribution within the sheet, which may result in varying availability on the surfaces of sheets depending on the pairing of constituent elements [20].

To quantify the charge accessible above each of the inspected TMD layer the planar average of the electron charge density across the supercell can be calculated. The obtained results for each one of the substrates are presented in a functions of height in Figure 7a. It is well visible, that the $MoSe_2$-related curve tops, with the WS_2 and MoS_2

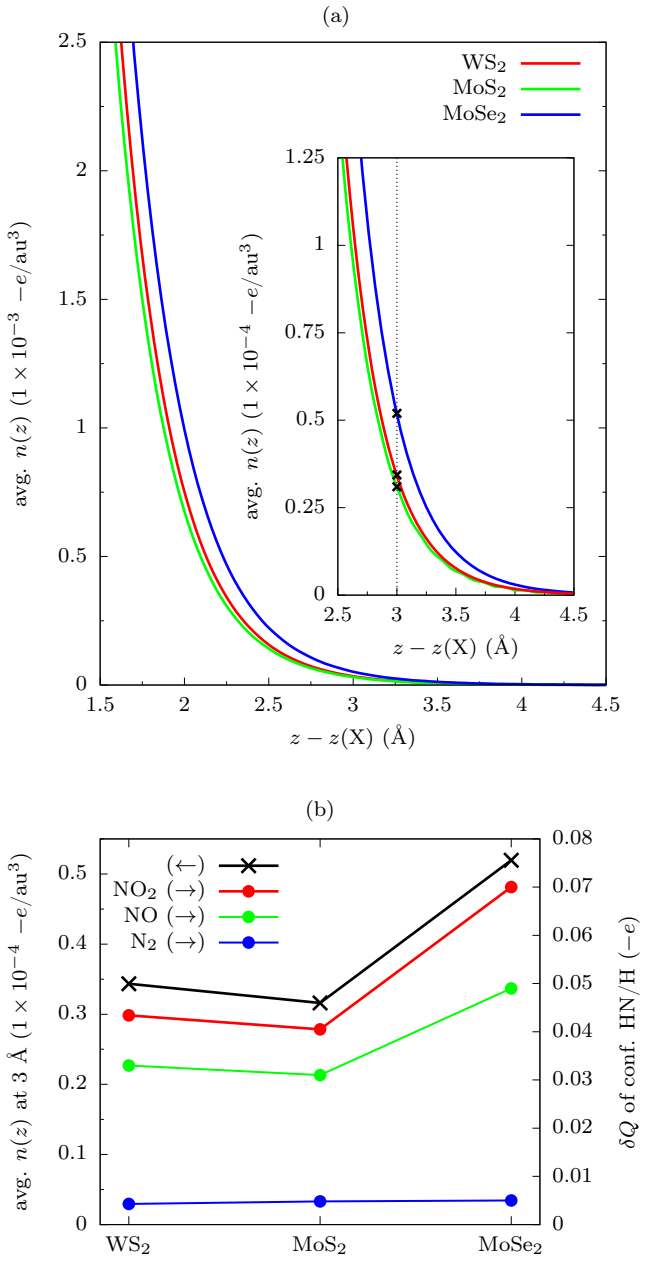

Figure 7: (a) Planar average of the electron charge density avg. $n(z)$ at heights relative to the TMD surface and (b) average electron charge density avg. $n(z)$ at 3 Å (x marks) compared with the average charge transfer δQ upon adsorption of NO_x for HN/N initial geometry systems (dot marks).

graphs situated in the middle and at the bottom respectively. That order is met for the whole domain of the functions, which includes the heights of adsorbing NO_x, typically 3–4 Å. Therefore, $MoSe_2$ provides the greatest charge to draw, followed by WS_2 and then MoS_2. The correlation between the above and charge transfer is illustrated by Figure 7b. For NO_2 the ordering of δQ magnitudes is the same as that of available charge. The NO transfers show similar dependence, however the TMD type has no impact on the transfers of N_2. As the amount of charge offered by a given TMD sheet has to be identical, the selectivity of enhanced adsorption interaction and higher charge transfer (see Figure 5) for different NO_x on the same kind of TMD has to be related to the molecule capability of accepting charge. The latter is a direct consequence of the adsorbate electronic properties.

Now, the high sensitivity of NO_2 to the TMD composition can be comfortably explained. An oxygen and nitrogen atoms, due to their valence structure, find themselves in the most energetically favorable position when participating in a double and triple bond respectively. Hence, the combination of two oxygen and one nitrogen atoms can hold additional negative charge, making NO_2 an excellent acceptor, ready to draw from the p_z orbitals projected by the chalcogens. Indeed, the intensity of NO_2-TMD interaction is directly correlated to the charge transfer, which is in turn highly dependent on the type of transition metal and chalcogen forming the TMD. This is clearly displayed by the obtained adsorption enhancements, as their NO_2-related levels correspond to increase in charge transfer (cf. Figure 6a and b). The NO case is a little more diverse. While the molecule acts like an acceptor, i.e. for the HN initial geometry, it is able to benefit from the greater adsorption interaction. However, when NO behaves more donor-like, the effect vanishes. This is displayed on the example of E_{ads} values related to the HO, VN and VO initial geometries, for whom the δQ levels are positive (cf. Figure 4a and b). For these, the E_{ads} ordering, related to the type of TMD and displayed by the HN system, does not appear. On average, the negative charge transfer predominates behavior of NO, generally making it able to participate in the effect, as it is visible in Figures 5 and 6. The case of N_2 is the most straightforward. Two nitrogen atoms form the molecule by a triple covalent bond, completely filling out their p orbitals. Therefore, N_2 is not involved in almost any charge transfer. Nevertheless, a careful observer may notice, that N_2in fact attracts an almost negligible, but nonzero, amount of charge, which should make it able to benefit a little from enhanced adsorption. Figure 6a seems to support this claim, however the magnitude of differences are almost identical, differing after the third decimal place. This makes enhancement so weak, that it can be assumed that N_2 does take part in it.

It should now be clear, that the selectivity of the enhanced adsorption is due to the level to which the molecule is able to behave as an acceptor with respect to the TMD sheet. Nevertheless, the unmissable is that the changes caused by the substitution of chalcogen are several times larger than those related to the swap of transition metal. Up to this point we have not touched on this important factor. The scale of the unevenness can be easily recognized by comparing the heights of Δ avg. $E_{ads}(MoS_2, WS_2)$ and Δavg. $E_{ads}(MoS_2, WS_2)$ histograms as seen in Figure 6a and b. As an acceptor interact with the TMD adsorbent mainly by drawing the projected charge in the form of the chalcogens p_z orbitals, the X atoms importance is somewhat intuitive. However, the metal impact on the adsorption remains fuzzy, alongside with the intrinsic origin of the enhancement connected to the characteristics of the M–X bond, specific to each TMD type. Therefore, we shall proceed to the last section, which addresses the above and elucidates the differences between WS_2, MoS_2, and $MoSe_2$ on the base of the chalcogen and transition metal interaction.

3.3. The enhanced adsorption dependence on transition metal vs. dichalcogen

The goal of this section is to unravel the relationship between the contribution of chalcogen and transition metal to the amount of charge accessible above a TMD layer. As it was highlighted in Section 3.2, the magnitude of the latter is responsible for the enhanced adsorption interaction occurring between acceptor molecule and a sheet, thus in this way we shall obtain the complete description of the effect.

Looking at Figure 6 it is evident, that the type of chalcogen has a much greater impact on the adsorption energy and charge transfer

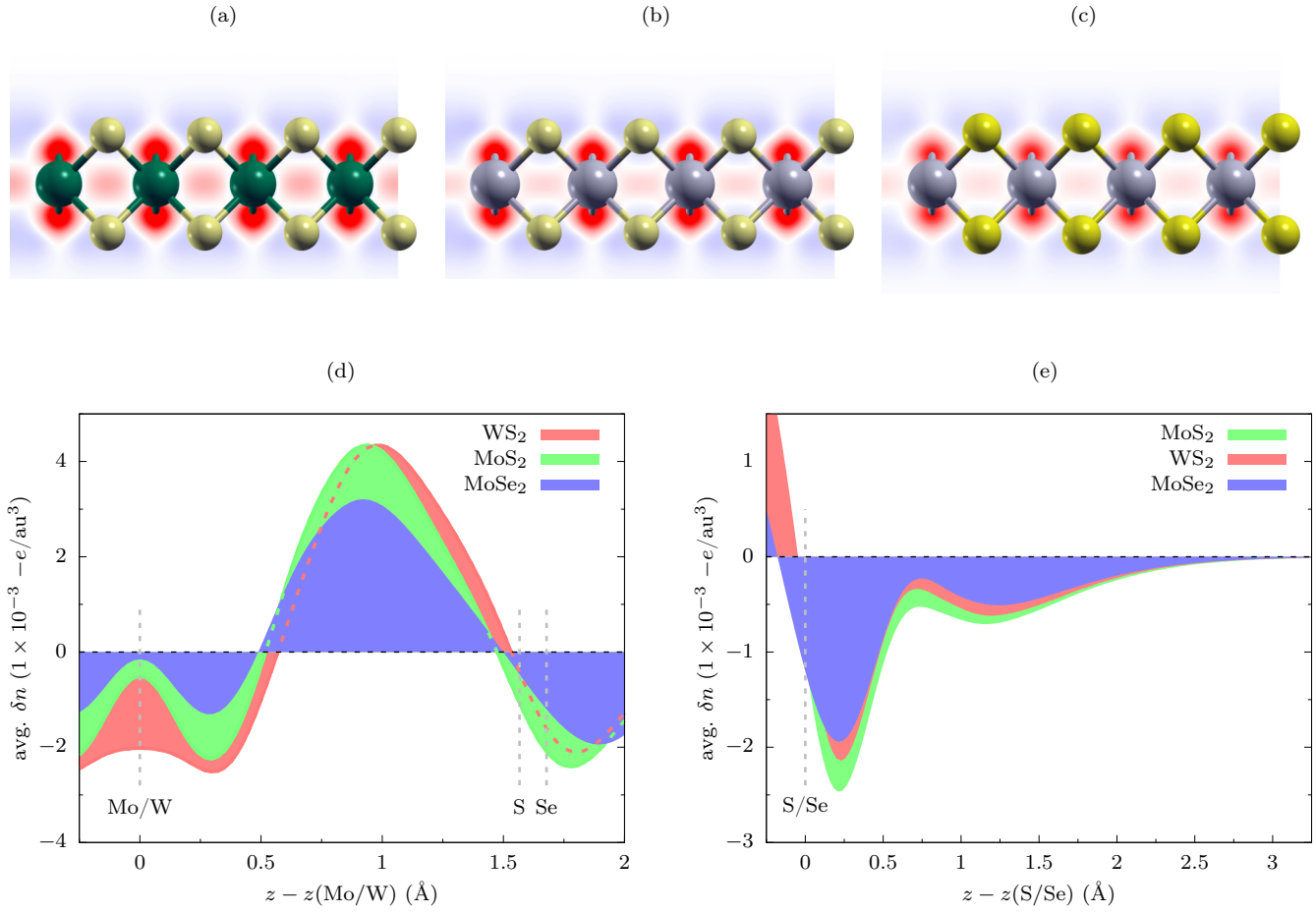

Figure 8: Electronic density of (a) MoS_2, (b) $MoSe_2$, and (c) $MoTe_2$ depleted of superposition of comprising elements atomic densities given by equation 5. Red and blue represent the increase and decrease in electron density, respectively. (d) Planar average of the charge difference avg. δn plotted as function of z-direction in relation to the transition-metal layer and (e) in relation to the upper chalcogen layer.

than the type of transition metal. It comes as no surprise, as the outwardly projected charge mostly depends on the chalcogens, however their behavior is to some extend dependent on the bonding with metal. Therefore the M atom type can also influence the TMD-adsorbate interaction, albeit far less, which can be easily recognized by comparing red and blue bars of NO_2 displayed in Figure 6). These dependencies can be further validated by Figure 7, which shows the electron charge density above the sheet increase much more for the chalcogen substitution S → Se (cf. MoS_2 and $MoSe_2$), than for the metal swap Mo → W (cf. MoS_2 and WS_2). To understand the mechanism governing the amount of this accessible charge, the M–X bond have to be examined.

The M–X bonding interaction leads to the accumulation of electronic charge between the atoms within the layer. Hence, it is only natural that this accumulation facilitates the depletion of charge projected outward. This, in turn, affects its availability on the surface of TMDs depending on their atomic composition. Therefore, it could be intuitively understood that factors such as binding energy, atomic distances relative to the covalent radii of the constituent elements, and their electronegativity may influence the redistribution of charge, and thus govern the underpinnings of the observed enhanced adsorption interaction for the acceptor type molecules. However, one can inspect the M–X interaction in a more detailed way by calculating charge density depleted of superposition of atomic densities

$$\delta n(\mathrm{X}) = n(\mathrm{MX_2}) - n(\mathrm{M}) - n(\mathrm{X}). \tag{5}$$

The obtained δn(X) for the centers of M–X bonds are showed in Figure 8a–c. Red and blue colors represent accordingly increase and decrease in electronic density with magnitude correlated to the color intensity. The analysis of the images display the covalent nature of the bonding, forming at the expense of disperse outward charge. The alterations in MoS_2 and WS_2 appear comparable, whereas $MoSe_2$ exhibits a notably lower accumulation of charge between bonded atoms. This aligns with the higher availability of electrons on the surface of $MoSe_2$. However, it is essential to note that this observation may be inadvertently influenced by the chosen placement of cross-sections, which may not fully represent changes in charge distribution due to M–X bonding.

To further substantiate the above findings, a more detailed examination of the M–X interaction is necessary. For this purpose, we have calculated the planar-averaged δn(X) densities, which are illustrated along the z-direction in relation to the transition-metal layer in Figure 8d and the upper chalcogen layer in Figure 8e. Upon inspecting the charge redistribution within the TMD monolayers (Figure 8d), the results reveal electron accumulation between atomic planes facilitated by charge depletion in their vicinity. Furthermore, the comparable accumulation between layers of transition metals and chalcogens in MoS_2 and WS_2 monolayers, and notably lower accumulation of charge between bonded atoms in $MoSe_2$ is observed. Additionally, the charge in WS_2 is shown to be shifted toward the surface when compared with MoS_2, despite the similar magnitude of accumulation. This is likely attributed to the larger size of W compared to Mo [55], necessitat-

ing charge distribution further from W, coupled with virtually identical interlayer spacing of Mo–S and of W–S. This, of course, indicates a greater overlap of orbitals in WS_2, coinciding with stronger atomic bonding (−7.16 eV), compared to that in MoS_2 (−6.69 eV). Conversely, both MoS_2 and $MoSe_2$ comprise Mo atoms. As a result, the maximum of electron accumulation occurs at the same distance from the transition metal, albeit with different values.

The described redistribution of charge within the TMD sheets also affects the electron density outside of them. To accommodate bond formation and the corresponding charge accumulation between atomic layers, all three monolayers experience charge depletion on their surface, as illustrated in Figure 8e. However, the extent of depletion differs between the sheets. $MoSe_2$ exhibits the least amount of electronic density loss on its surface, which aligns with its lower accumulation within the monolayer. On the other hand, both MoS_2 and WS_2 experience comparable higher accumulation, coinciding with a greater depletion of electronic density outside of the sheet relative to $MoSe_2$. However, the results also indicate a difference between the two monolayers, despite the comparable accumulation and the same chalcogen comprising them. This disparity likely originates from differences in charge distribution within the sheet. On one hand, there is a larger depletion of charge on the atomic plane of W than Mo, and on the other, the accumulated charge is closer to the surface in WS_2 than MoS_2. Therefore, there is less demand for charge shifting from the surface in the former than the latter.

Taken together, the heightened availability of charge on the surface of $MoSe_2$ compared to the monolayers of WS_2 and MoS_2 can be attributed to a combination of low electron depletion on its surface (characteristic of Mo–Se bonding) and a generally greater projection of charge from $4p$ orbitals in Se compared to $3p$ orbitals in S. Conversely, the smaller difference in availability between WS_2 and MoS_2 is facilitated by the disparities in atomic bonding. These differences enable the accumulation of charge within the sheet closer to the surface in the case of WS_2. As a result, the intrinsic features of M–X bonding are the underpinnings behind the enhanced adsorption interaction of acceptor-type molecules.

4. Conclusions

The present paper utilizes the density functional theory approach to predict the role of transition metal and chalcogen atom in adsorption of NO_2, NO, and N_2 on monolayers of MoS_2, $MoSe_2$, and WS_2 transition-metal dichalcogenides. The key characteristics of each such process are summarized in Table 1. The results confirms the previous assumption [20], that only the acceptor-acting molecules adsorbing on TMD layers are able to benefit from enhanced adsorption interaction. The magnitude of the latter is mostly impacted by the chalcogen type and not so much by the kind of transition metal comprising the sheet, which is best visible in Figure 6. As the calculations were carefully conducted for various initial conformations of each adsorbing molecule, we exclude the geometry-related origin of the observed differences and relate it to the intrinsic nature of a given TMD layer. The average adsorption energy of NO_2 rises only by about 3.7 % upon substitution of Mo with W and by as much as 26.7 % after swapping S with Se atom, relative to the interaction with MoS_2. The molecule of NO experiences diminished effect, as it does accept less charge and only in some of its configurations. Finally, N_2 is practically indifferent to the TMD composition. Above outcomes can be easily appreciated by looking at Figure 5).

The observed enhancement of acceptor molecules adsorption is directly related with the amount of accessible charge located above the TMD surface. The latter is dependent on the transition metal–chalcogen covalent bonding. We reveal, that the stronger binding demands higher electronic density localized between metal and chalcogen atoms, coming at the expense of charge otherwise dispersed outside the material. Naturally, the former varies according to the type of metal and chalcogen forming the sheet (see Figure 7 and 8). It was shown previously, that the higher electronegativity of the chalcogen results in greater accumulation of electrons within the TMD body [20], however the current study examines the significance of the different types of transition metals was examined for the first time. Contrary to the hitherto belief, the substitution with more electronegative metal does not diminish, but increase the available surface charge, which was inspected on the example of MoS_2 compared to WS_2. This is due to the W–S bond being weaker than Mo–S and needing less charge to form. The size effects of the atoms also play a certain role, however a minor one. Nevertheless, the differences between MoS_2 and WS_2 are several (up to more than seven) times smaller than those observed for TMD containing disparate chalcogens. The comparison of MoS_2 and $MoSe_2$ leads to the conclusion, that the chalcogen kind is of far greater importance for enhancing the interaction with acceptor molecules. This is unexpected, as S (2.58) differs in electronegativity from Se (2.55) much less than Mo (2.16) from W (2.36) atom. These findings show, that during the evaluation of the adsorption processes including given TMD sheet one has to specifically consider its metal–chalcogen bond.

With the in-depth knowledge of the mechanism responsible for the NO_x-TMD interaction, one can leverage the layer composition-adsorption relationships in order to obtain gas sensor with well tailored sensitivity and recovery. Moreover, the various responses of the different sheets allow for enhanced specificity of detection, addressing a key limitation of semiconductor sensors [56–60]. This is of considerable importance, as the latter often respond to multiple species, distinguishing between which can be difficult. Such cross-sensitivity can lead to false positives or negatives, undesirable in gas detection.

Acknowledgments

This work was supported by the Ministry of Education and Science in Poland (Grant No. 0512/SBAD/2320) within the project realized at the Institute of Physics, Poznan University of Technology. Computations reported in this work have been performed at Poznan Supercomputing and Networking Center (PSNC) under Grant No. 608.

References

[1] R. Atkinson, Atmospheric chemistry of VOCs and NO_x, Atmospheric Environment 34 (12) (2000) 2063–2101. doi:https://doi.org/10.1016/S1352-2310(99)00460-4.
URL https://www.sciencedirect.com/science/article/pii/S1352231099004604

[2] A. F. Stein, D. Lamb, Empirical evidence for the low- and high-NO_x photochemical regimes of sulfate and nitrate formation, Atmospheric Environment 37 (26) (2003) 3615–3625. doi:https://doi.org/10.1016/S1352-2310(03)00458-8.
URL https://www.sciencedirect.com/science/article/pii/S1352231003004588

[3] M. Tajuelo, A. Rodríguez, M. T. Baeza-Romero, A. Aranda, Y. D. de Mera, D. Rodríguez, Secondary organic aerosol formation from α-methylstyrene atmospheric degradation: Role of NO_x level, relative humidity and inorganic seed aerosol, Atmospheric Research 230 (2019) 104631. doi:https://doi.org/10.1016/j.atmosres.2019.104631.
URL https://www.sciencedirect.com/science/article/pii/S0169809519306878

[4] C. Yan, W. Nie, A. L. Vogel, L. Dada, K. Lehtipalo, D. Stolzenburg, R. Wagner, M. P. Rissanen, M. Xiao, L. Ahonen, L. Fischer, C. Rose, F. Bianchi, H. Gordon, M. Simon, M. Heinritzi, O. Garmash, P. Roldin, A. Dias, P. Ye, V. Hofbauer, A. Amorim, P. S. Bauer, A. Bergen, A.-K. Bernhammer, M. Breitenlechner, S. Brilke, A. Buchholz, S. B. Mazon, M. R. Canagaratna, X. Chen, A. Ding, J. Dommen, D. C. Draper, J. Duplissy, C. Frege, C. Heyn, R. Guida, J. Hakala, L. Heikkinen, C. R. Hoyle, T. Jokinen, J. Kangasluoma, J. Kirkby, J. Kontkanen, A. Kürten, M. J. Lawler, H. Mai, S. Mathot, R. L. Mauldin, U. Molteni, L. Nichman, T. Nieminen, J. Nowak, A. Ojdanic, A. Onnela, A. Pajunoja, T. Petäjä, F. Piel, L. L. J. Quéléver, N. Sarnela, S. Schallhart, K. Sengupta, M. Sipilä, A. Tomé, J. Tröstl, O. Väisänen, A. C. Wagner, A. Ylisirniö, Q. Zha, U. Baltensperger, K. S. Carslaw, J. Curtius, R. C. Flagan, A. Hansel, I. Riipinen, J. N. Smith, A. Virtanen, P. M. Winkler, N. M. Donahue, V.-M. Kerminen, M. Kulmala, M. Ehn, D. R. Worsnop, Size-dependent influence of NO_x on the growth rates of organic aerosol particles, Science Advances 6 (22) (2020) eaay4945. arXiv:https://www.science.org/doi/pdf/10.1126/sciadv.aay4945, doi:10.1126/sciadv.aay4945.
URL https://www.science.org/doi/abs/10.1126/sciadv.aay4945

[5] L. Xu, N. T. Tsona, B. You, Y. Zhang, S. Wang, Z. Yang, L. Xue, L. Du, NO_x enhances secondary organic aerosol formation from nighttime γ-terpinene ozonolysis, Atmospheric Environment 225 (2020) 117375. doi:https://doi.org/10.1016/j.atmosenv.2020.117375.
URL https://www.sciencedirect.com/science/article/pii/S135223102030114X

[6] S. Wang, N. T. Tsona, L. Du, Effect of NO_x on secondary organic aerosol formation from the photochemical transformation of allyl acetate, Atmospheric Environment 255 (2021) 118426. doi:https://doi.org/10.1016/j.atmosenv.2021.118426.
URL https://www.sciencedirect.com/science/article/pii/S1352231021002454

[7] L. Stockfelt, E. M. Andersson, P. Molnár, A. Rosengren, L. Wilhelmsen, G. Sallsten, L. Barregard, Long term effects of residential NO_x exposure on total and cause-specific mortality and incidence of myocardial infarction in a swedish cohort, Environmental Research 142 (2015) 197–206. doi:https://doi.org/10.1016/j.envres.2015.06.045.
URL https://www.sciencedirect.com/science/article/pii/S0013935115300190

[8] P. E. Pfeffer, G. C. Donaldson, A. J. Mackay, J. A. Wedzicha, Increased chronic obstructive pulmonary disease exacerbations of likely viral etiology follow elevated ambient nitrogen oxides, American Journal of Respiratory and Critical Care Medicine 199 (5) (2019) 581–591, pMID: 30157387. arXiv:https://doi.org/10.1164/rccm.201712-2506OC, doi:10.1164/rccm.201712-2506OC.
URL https://doi.org/10.1164/rccm.201712-2506OC

[9] M. Kowalska, M. Skrzypek, M. Kowalski, J. Cyrys, Effect of NO_x and NO_2 concentration increase in ambient air to daily bronchitis and asthma exacerbation, Silesian Voivodeship in Poland, International Journal of Environmental Research and Public Health 17 (3) (2020). doi:10.3390/ijerph17030754.
URL https://www.mdpi.com/1660-4601/17/3/754

[10] S. Shaw, B. Van Heyst, An evaluation of risk ratios on physical and mental health correlations due to increases in ambient nitrogen oxide (NO_x) concentrations, Atmosphere 13 (6) (2022). doi:10.3390/atmos13060967.
URL https://www.mdpi.com/2073-4433/13/6/967

[11] D. L. Mauzerall, B. Sultan, N. Kim, D. F. Bradford, NO_x emissions from large point sources: variability in ozone production, resulting health damages and economic costs, Atmospheric Environment 39 (16) (2005) 2851–2866. doi:https://doi.org/10.1016/j.atmosenv.2004.12.041.
URL https://www.sciencedirect.com/science/article/pii/S1352231005000907

[12] H. Michiels, I. Mayeres, L. Int Panis, L. De Nocker, F. Deutsch, W. Lefebvre, PM2.5 and NO_x from traffic: Human health impacts, external costs and policy implications from the Belgian perspective, Transportation Research Part D: Transport and Environment 17 (8) (2012) 569–577. doi:https://doi.org/10.1016/j.trd.2012.07.001.
URL https://www.sciencedirect.com/science/article/pii/S1361920912000740

[13] K. R. Bilsback, D. Kerry, B. Croft, B. Ford, S. H. Jathar, E. Carter, R. V. Martin, J. R. Pierce, Beyond SO_x reductions from shipping: assessing the impact of NO_x and carbonaceous-particle controls on human health and climate, Environmental Research Letters 15 (12) (2020) 124046. doi:10.1088/1748-9326/abc718.
URL https://dx.doi.org/10.1088/1748-9326/abc718

[14] Y. Guo, L. Zhu, X. Wang, X. Qiu, W. Qian, L. Wang, Assessing environmental impact of NO_x and SO_2 emissions in textiles production with chemical footprint, Science of The Total Environment 831 (2022) 154961. doi:https://doi.org/10.1016/j.scitotenv.2022.154961.
URL https://www.sciencedirect.com/science/article/pii/S004896972202054X

[15] U. Asghar, S. Rafiq, A. Anwar, T. Iqbal, A. Ahmed, F. Jamil, M. S. Khurram, M. M. Akbar, A. Farooq, N. S. Shah, Y.-K. Park, Review on the progress in emission control technologies for the abatement of CO_2, SO_x and NO_x from fuel combustion, Journal of Environmental Chemical Engineering 9 (5) (2021) 106064. doi:https://doi.org/10.1016/j.jece.2021.106064.
URL https://www.sciencedirect.com/science/article/pii/S2213343721010411

[16] V. Babar, H. Vovusha, U. Schwingenschlögl, Density functional theory analysis of gas adsorption on monolayer and few layer transition metal dichalcogenides: Implications for sensing, ACS Applied Nano Materials 2 (9) (2019) 6076–6080. arXiv:https://doi.org/10.1021/acsanm.9b01642, doi:10.1021/acsanm.9b01642.
URL https://doi.org/10.1021/acsanm.9b01642

[17] V. M. Bermudez, Computational study of the adsorption of NO_2 on monolayer MoS_2, The Journal of Physical Chemistry C 124 (28) (2020) 15275–15284. arXiv:https://doi.org/10.1021/acs.jpcc.0c03786, doi:10.1021/acs.jpcc.0c03786.
URL https://doi.org/10.1021/acs.jpcc.0c03786

[18] V. M. Bermudez, Theoretical study of the adsorption of Lewis acids on MoS_2 in relation to atomic layer deposition of Al_2O_3, Journal of Vacuum Science & Technology A 38 (6) (2020) 062412. arXiv:https://pubs.aip.org/avs/jva/article-pdf/doi/10.1116/6.0000467/15819780/062412_1_online.pdf, doi:10.1116/6.0000467.
URL https://doi.org/10.1116/6.0000467

[19] M. J. Szary, Dative bonding as a mechanism for enhanced catalysis on the surface of MoS_2, Applied Surface Science 630 (2023) 157462. doi:https://doi.org/10.1016/j.apsusc.2023.157462.
URL https://www.sciencedirect.com/science/article/pii/S0169433223011406

[20] M. J. Szary, P. Radomski, Unveiling the chemical underpinnings behind the enhanced adsorption interaction of NO_2 on MoS_2, $MoSe_2$, and $MoTe_2$ transition metal dichalcogenides, The Journal of Physical Chemistry C 127 (43) (2023) 21374–21386. arXiv:https://doi.org/10.1021/acs.jpcc.3c05101, doi:10.1021/acs.jpcc.3c05101.
URL https://doi.org/10.1021/acs.jpcc.3c05101

[21] M. Donarelli, S. Prezioso, F. Perrozzi, F. Bisti, M. Nardone, L. Giancaterini, C. Cantalini, L. Ottaviano, Response to NO_2 and other gases of resistive chemically exfoliated MoS_2-based gas sensors, Sensors and Actuators B: Chemical 207 (2015) 602–613. doi:https://doi.org/10.1016/j.snb.2014.10.099.
URL https://www.sciencedirect.com/science/article/pii/S0925400514013112

[22] T. Xu, Y. Pei, Y. Liu, D. Wu, Z. Shi, J. Xu, Y. Tian, X. Li, High-response NO_2 resistive gas sensor based on bilayer MoS_2 grown by a new two-step chemical vapor deposition method, Journal of Alloys and Compounds 725 (2017) 253–259. doi:https://doi.org/10.1016/j.jallcom.2017.06.105.
URL https://www.sciencedirect.com/science/article/pii/S0925838817321047

[23] X. Chen, X. Chen, Y. Han, C. Su, M. Zeng, N. Hu, Y. Su, Z. Zhou, H. Wei, Z. Yang, Two-dimensional $MoSe_2$ nanosheets via liquid-phase exfoliation for high-performance room temperature NO_2 gas sensors, Nanotechnology 30 (44) (2019) 445503. doi:10.1088/1361-6528/ab35ec.
URL https://dx.doi.org/10.1088/1361-6528/ab35ec

[24] Z. Feng, Y. Xie, J. Chen, Y. Yu, S. Zheng, R. Zhang, Q. Li, X. Chen, C. Sun, H. Zhang, W. Pang, J. Liu, D. Zhang, Highly sensitive $MoTe_2$ chemical sensor with fast recovery rate through gate biasing, 2D Materials 4 (2) (2017) 025018. doi:10.1088/2053-1583/aa57fe.

URL https://dx.doi.org/10.1088/2053-1583/aa57fe

[25] J. Baek, D. Yin, N. Liu, I. Omkaram, C. Jung, H. Im, S. Hong, S. M. Kim, Y. K. Hong, J. Hur, Y. Yoon, S. Kim, A highly sensitive chemical gas detecting transistor based on highly crystalline CVD-grown $MoSe_2$ films, Nano Research 10 (6) (2017) 1861–1871. doi:10.1007/s12274-016-1291-7.
URL https://doi.org/10.1007/s12274-016-1291-7

[26] R. Kumar, N. Goel, M. Kumar, UV-activated MoS_2 based fast and reversible NO_2 sensor at room temperature, ACS Sensors 2 (11) (2017) 1744–1752, pMID: 29090571. arXiv:https://doi.org/10.1021/acssensors.7b00731, doi:10.1021/acssensors.7b00731.
URL https://doi.org/10.1021/acssensors.7b00731

[27] E. Wu, Y. Xie, B. Yuan, H. Zhang, X. Hu, J. Liu, D. Zhang, Ultrasensitive and fully reversible NO_2 gas sensing based on p-type $MoTe_2$ under ultraviolet illumination, ACS Sensors 3 (9) (2018) 1719–1726, pMID: 30105902. doi:10.1021/acssensors.8b00461.
URL https://doi.org/10.1021/acssensors.8b00461

[28] T. Pham, G. Li, E. Bekyarova, M. E. Itkis, A. Mulchandani, MoS_2-based optoelectronic gas sensor with sub-parts-per-billion limit of NO_2 gas detection, ACS Nano 13 (3) (2019) 3196–3205. doi:10.1021/acsnano.8b08778.
URL https://doi.org/10.1021/acsnano.8b08778

[29] Y. Tang, Y. Zhao, H. Liu, Room-temperature semiconductor gas sensors: Challenges and opportunities, ACS Sensors 7 (12) (2022) 3582–3597, pMID: 36399520. arXiv:https://doi.org/10.1021/acssensors.2c01142, doi:10.1021/acssensors.2c01142.
URL https://doi.org/10.1021/acssensors.2c01142

[30] Z. Wang, M. Bu, N. Hu, L. Zhao, An overview on room-temperature chemiresistor gas sensors based on 2D materials: Research status and challenge, Composites Part B: Engineering 248 (2023) 110378. doi:https://doi.org/10.1016/j.compositesb.2022.110378.
URL https://www.sciencedirect.com/science/article/pii/S135983682200751X

[31] S. Aftab, M. Zahir Iqbal, S. Hussain, H. H. Hegazy, F. Kabir, S. Hassan Abbas Jaffery, G. Koyyada, New developments in gas sensing using various two-dimensional architectural designs, Chemical Engineering Journal 469 (2023) 144039. doi:https://doi.org/10.1016/j.cej.2023.144039.
URL https://www.sciencedirect.com/science/article/pii/S1385894723027705

[32] W. S. Yun, S. W. Han, S. C. Hong, I. G. Kim, J. D. Lee, Thickness and strain effects on electronic structures of transition metal dichalcogenides: 2h-mX_2 semiconductors (m = mo, w; x = s, se, te), Phys. Rev. B 85 (2012) 033305. doi:10.1103/PhysRevB.85.033305.
URL https://link.aps.org/doi/10.1103/PhysRevB.85.033305

[33] Y. Zeng, S. Lin, D. Gu, X. Li, Two-dimensional nanomaterials for gas sensing applications: The role of theoretical calculations, Nanomaterials 8 (10) (2018). doi:10.3390/nano8100851.
URL https://www.mdpi.com/2079-4991/8/10/851

[34] X. Tang, A. Du, L. Kou, Gas sensing and capturing based on two-dimensional layered materials: Overview from theoretical perspective, WIREs Computational Molecular Science 8 (4) (2018) e1361. arXiv:https://wires.onlinelibrary.wiley.com/doi/pdf/10.1002/wcms.1361, doi:https://doi.org/10.1002/wcms.1361.
URL https://wires.onlinelibrary.wiley.com/doi/abs/10.1002/wcms.1361

[35] J. Cao, J. Zhou, J. Chen, W. Wang, Y. Zhang, X. Liu, Effects of phase selection on gas-sensing performance of MoS_2 and WS_2 substrates, ACS Omega 5 (44) (2020) 28823–28830, pMID: 33195935. doi:10.1021/acsomega.0c04176.
URL https://doi.org/10.1021/acsomega.0c04176

[36] E. Salih, A. I. Ayesh, First principle study of transition metals codoped MoS_2 as a gas sensor for the detection of NO and NO_2 gases, Physica E: Low-dimensional Systems and Nanostructures 131 (2021) 114736. doi:https://doi.org/10.1016/j.physe.2021.114736.
URL https://www.sciencedirect.com/science/article/pii/S1386947721001193

[37] E. Piosik, M. J. Szary, Development of MoS_2 doping strategy for enhanced SO_2 detection at room temperature, Applied Surface Science 638 (2023) 158013. doi:https://doi.org/10.1016/j.apsusc.2023.158013.
URL https://www.sciencedirect.com/science/article/pii/S0169433223016926

[38] P. Giannozzi, S. Baroni, N. Bonini, M. Calandra, R. Car, C. Cavazzoni, D. Ceresoli, G. L. Chiarotti, M. Cococcioni, I. Dabo, A. D. Corso, S. de Gironcoli, S. Fabris, G. Fratesi, R. Gebauer, U. Gerstmann, C. Gougoussis, A. Kokalj, M. Lazzeri, L. Martin-Samos, N. Marzari, F. Mauri, R. Mazzarello, S. Paolini, A. Pasquarello, L. Paulatto, C. Sbraccia, S. Scandolo, G. Sclauzero, A. P. Seitsonen, A. Smogunov, P. Umari, R. M. Wentzcovitch, QUANTUM ESPRESSO: a modular and open-source software project for quantum simulations of materials, Journal of Physics: Condensed Matter 21 (39) (2009) 395502. doi:10.1088/0953-8984/21/39/395502.
URL https://doi.org/10.1088%2F0953-8984%2F21%2F39%2F395502

[39] P. Giannozzi, O. Andreussi, T. Brumme, O. Bunau, M. B. Nardelli, M. Calandra, R. Car, C. Cavazzoni, D. Ceresoli, M. Cococcioni, N. Colonna, I. Carnimeo, A. D. Corso, S. de Gironcoli, P. Delugas, R. A. D. Jr, A. Ferretti, A. Floris, G. Fratesi, G. Fugallo, R. Gebauer, U. Gerstmann, F. Giustino, T. Gorni, J. Jia, M. Kawamura, H.-Y. Ko, A. Kokalj, E. Küçükbenli, M. Lazzeri, M. Marsili, N. Marzari, F. Mauri, N. L. Nguyen, H.-V. Nguyen, A. O. de-la Roza, L. Paulatto, S. Poncé, D. Rocca, R. Sabatini, B. Santra, M. Schlipf, A. P. Seitsonen, A. Smogunov, I. Timrov, T. Thonhauser, P. Umari, N. Vast, X. Wu, S. Baroni, Advanced capabilities for materials modelling with QUANTUM ESPRESSO, Journal of Physics: Condensed Matter 29 (46) (2017) 465901.
URL http://stacks.iop.org/0953-8984/29/i=46/a=465901

[40] P. Giannozzi, O. Baseggio, P. Bonfà, D. Brunato, R. Car, I. Carnimeo, C. Cavazzoni, S. de Gironcoli, P. Delugas, F. Ferrari Ruffino, A. Ferretti, N. Marzari, I. Timrov, A. Urru, S. Baroni, QUANTUM ESPRESSO toward the exascale, The Journal of Chemical Physics 152 (15) (2020) 154105. arXiv:https://doi.org/10.1063/5.0005082, doi:10.1063/5.0005082.
URL https://doi.org/10.1063/5.0005082

[41] J. P. Perdew, K. Burke, M. Ernzerhof, Generalized gradient approximation made simple, Phys. Rev. Lett. 77 (1996) 3865–3868. doi:10.1103/PhysRevLett.77.3865.
URL https://link.aps.org/doi/10.1103/PhysRevLett.77.3865

[42] J. P. Perdew, A. Ruzsinszky, G. I. Csonka, O. A. Vydrov, G. E. Scuseria, L. A. Constantin, X. Zhou, K. Burke, Restoring the density-gradient expansion for exchange in solids and surfaces, Phys. Rev. Lett. 100 (2008) 136406. doi:10.1103/PhysRevLett.100.136406.
URL https://link.aps.org/doi/10.1103/PhysRevLett.100.136406

[43] S. Grimme, Semiempirical GGA-type density functional constructed with a long-range dispersion correction, Journal of Computational Chemistry 27 (15) (2006) 1787–1799. arXiv:https://onlinelibrary.wiley.com/doi/pdf/10.1002/jcc.20495, doi:10.1002/jcc.20495.
URL https://onlinelibrary.wiley.com/doi/abs/10.1002/jcc.20495

[44] S. Grimme, J. Antony, S. Ehrlich, H. Krieg, A consistent and accurate ab initio parametrization of density functional dispersion correction (DFT-D) for the 94 elements H-Pu, The Journal of Chemical Physics 132 (15) (2010) 154104. arXiv:https://doi.org/10.1063/1.3382344, doi:10.1063/1.3382344.
URL https://doi.org/10.1063/1.3382344

[45] J. Heyd, G. E. Scuseria, M. Ernzerhof, Hybrid functionals based on a screened coulomb potential, The Journal of Chemical Physics 118 (18) (2003) 8207–8215. arXiv:https://pubs.aip.org/aip/jcp/article-pdf/118/18/8207/10847843/8207_1_online.pdf, doi:10.1063/1.1564060.
URL https://doi.org/10.1063/1.1564060

[46] A. Tkatchenko, M. Scheffler, Accurate molecular van der waals interactions from ground-state electron density and free-atom reference data, Phys. Rev. Lett. 102 (2009) 073005. doi:10.1103/PhysRevLett.102.073005.
URL https://link.aps.org/doi/10.1103/PhysRevLett.102.073005

[47] S. Zhao, J. Xue, W. Kang, Gas adsorption on MoS_2 monolayer from first-principles calculations, Chemical Physics Letters 595-596 (2014) 35–42. doi:https://doi.org/10.1016/j.cplett.2014.01.043.

URL https://www.sciencedirect.com/science/article/pii/S0009261414000529
[48] M. J. Szary, Computational study of the intercalation of NO_2 between bilayer $MoTe_2$, Applied Surface Science 611 (2023) 155514. doi:https://doi.org/10.1016/j.apsusc.2022.155514.
URL https://www.sciencedirect.com/science/article/pii/S0169433222030422
[49] L. Zhu, C. Qin, Y. Wang, J. Cao, Single-atom Pt supported on non-metal doped WS_2 for photocatalytic CO_2 reduction: A first-principles study, Applied Surface Science 626 (2023) 157252. doi:https://doi.org/10.1016/j.apsusc.2023.157252.
URL https://www.sciencedirect.com/science/article/pii/S0169433223009303
[50] J. Liu, T. Shen, J.-C. Ren, S. Li, W. Liu, Role of van der waals interactions on the binding energies of 2D transition-metal dichalcogenides, Applied Surface Science 608 (2023) 155163. doi:https://doi.org/10.1016/j.apsusc.2022.155163.
URL https://www.sciencedirect.com/science/article/pii/S0169433222026915
[51] H. J. Monkhorst, J. D. Pack, Special points for brillouin-zone integrations, Phys. Rev. B 13 (1976) 5188–5192. doi:10.1103/PhysRevB.13.5188.
URL https://link.aps.org/doi/10.1103/PhysRevB.13.5188
[52] H. Cui, J. Jiang, C. Gao, F. Dai, J. An, Z. Wen, Y. Liu, DFT study of Cu-modified and Cu-embedded WSe_2 monolayers for cohesive adsorption of NO_2, SO_2, CO_2, and H_2S, Applied Surface Science 583 (2022) 152522. doi:https://doi.org/10.1016/j.apsusc.2022.152522.
URL https://www.sciencedirect.com/science/article/pii/S0169433222001076
[53] L. Bengtsson, Dipole correction for surface supercell calculations, Phys. Rev. B 59 (1999) 12301–12304. doi:10.1103/PhysRevB.59.12301.
URL https://link.aps.org/doi/10.1103/PhysRevB.59.12301
[54] A. Kokalj, XCrySDen–a new program for displaying crystalline structures and electron densities, Journal of Molecular Graphics and Modelling 17 (3) (1999) 176 – 179. doi:https://doi.org/10.1016/S1093-3263(99)00028-5.
URL http://www.sciencedirect.com/science/article/pii/S1093326399000285
[55] B. Cordero, V. Gómez, A. E. Platero-Prats, M. Revés, J. Echeverría, E. Cremades, F. Barragán, S. Alvarez, Covalent radii revisited, Dalton Trans. (2008) 2832–2838doi:10.1039/B801115J.
URL http://dx.doi.org/10.1039/B801115J
[56] S. Morrison, Selectivity in semiconductor gas sensors, Sensors and Actuators 12 (4) (1987) 425–440. doi:https://doi.org/10.1016/0250-6874(87)80061-6.
URL https://www.sciencedirect.com/science/article/pii/0250687487800616
[57] J. Viricelle, A. Pauly, L. Mazet, J. Brunet, M. Bouvet, C. Varenne, C. Pijolat, Selectivity improvement of semi-conducting gas sensors by selective filter for atmospheric pollutants detection, Materials Science and Engineering: C 26 (2) (2006) 186–195, selected Papers Presented at the MADICA 2004 Conference, Fourth Maghreb-Europe Meeting on Materials and their Applications for Devices and Physical, Chemical and Biological Sensors Tunis-Ghammart, Tunisia, 29 November- 1 December 2004. doi:https://doi.org/10.1016/j.msec.2005.10.062.
URL https://www.sciencedirect.com/science/article/pii/S0928493105004418
[58] A. Dey, Semiconductor metal oxide gas sensors: A review, Materials Science and Engineering: B 229 (2018) 206–217. doi:https://doi.org/10.1016/j.mseb.2017.12.036.
URL https://www.sciencedirect.com/science/article/pii/S0921510717303574
[59] Z. Li, H. Li, Z. Wu, M. Wang, J. Luo, H. Torun, P. Hu, C. Yang, M. Grundmann, X. Liu, Y. Fu, Advances in designs and mechanisms of semiconducting metal oxide nanostructures for high-precision gas sensors operated at room temperature, Mater. Horiz. 6 (2019) 470–506. doi:10.1039/C8MH01365A.
URL http://dx.doi.org/10.1039/C8MH01365A
[60] J. Wawrzyniak, Advancements in improving selectivity of metal oxide semiconductor gas sensors opening new perspectives for their application in food industry, Sensors 23 (23) (2023). doi:10.3390/s23239548.
URL https://www.mdpi.com/1424-8220/23/23/9548